14th International Symposium on Turbulence and Shear Flow Phenomena (TSFP14)
Heidelberg, Germany, July 28–31, 2026

DNS STUDY OF TURBULENT FLOW THROUGH A SLANTED DUCT

Rafae A. Shami, Taylor C. Opperman, and Bing-Chen Wang
Department of Mechanical Engineering
University of Manitoba
Winnipeg, MB, R3T 5V6, Canada
shamir@myumanitoba.ca, BingChen.Wang@umanitoba.ca

Mark S. Tachie
Department of Mechanical Engineering
The University of Melbourne
Melbourne, Victoria 3010, Australia
mark.tachie@student.unimelb.edu.au

ABSTRACT

Turbulent flow through a slanted duct is investigated using direct numerical simulations (DNS) for three slant angles, $\alpha = 15^\circ$, 30°, and 45°, at $Re_\tau = 300$. The effects of slant angle are systematically analyzed by examining first- and second-order statistical moments, Reynolds-stress budget balances, and premultiplied energy spectra. Secondary flows of Prandtl's second kind manifest as four pairs of counter-rotating mean vortices in each corner of the slanted duct. In the slanted-duct flows, enhanced boundary layer interaction occurs in the acute corners. Accordingly, the intensity of the cross-stream motions are augmented significantly compared to the orthogonal square-duct flow case. A redistribution of turbulence kinetic energy (TKE) toward the obtuse corner is also observed, driven by enhancement of turbulent shear stress in the obtuse corner and dampening in the acute. In general, the turbulent statistics follow this enhancement and dampening trend.

INTRODUCTION

Square-duct flows are relevant in practical engineering applications, including heat exchangers and heating, ventilation, and air conditioning (HVAC) systems. A conventional orthogonal square-duct flow exhibits four symmetric counter-rotating vortex pairs that transport high-momentum fluid from the duct core toward the corners. When a slant angle α is introduced, symmetry about the horizontal and vertical planes is broken, producing distinct obtuse- and acute-corners. This geometric modification generates coexisting regions of strong and weak boundary-layer interactions that significantly alters the mean secondary flows and turbulence structures relative to the orthogonal square-duct flow.

Gessner & Jones (1973) conducted hot-wire experiments on turbulent square-duct flows. They observed the formation of secondary flows in square ducts and related their origin to the imbalance between Reynolds stresses and static pressure gradients. Gavrilakis (1992) performed DNS of turbulent square-duct flow and showed that secondary flows affect the distribution of the wall shear stress. He also observed that the maximum magnitude of the cross-stream velocity was 1–2% of the bulk flow in the near-wall region. Huser *et al.* (1994) examined the Reynolds stress transport equation of a square-duct flow using DNS. They found that, away from the corners, the turbulence dynamics resemble those of plane channel flow, Meanwhile, they found that the corner regions of the duct were characterized by increased turbulence transport and redistribution compared to a plane-channel flow.

Studies of other non-circular cross-sections reveal that the secondary flow vortex centers, turbulent structures, and occurrence of local laminarization are sensitive to the cross-sectional geometry of a duct (Vinuesa *et al.*, 2014; Nikitin & Yakhot, 2005).

While orthogonal square ducts have been studied extensively, studies on the effect of slant angle α on the flow physics of square-duct flow are scarce (Raiesi *et al.*, 2011; Fukushima & Kasagi, 2003). In view of this knowledge gap, the present study aims to perform a detailed DNS investigation of the effects of slanting the duct sidewalls on the mean pattern of the secondary flows, shear-stress distribution, and turbulence kinetic energy (TKE) budget balance.

TEST CASE AND NUMERICAL ALGORITHM

Figure 1 shows the computational domain and coordinate system of the slanted-duct flows. Here, the spanwise, vertical, and streamwise coordinates are represented by x, y, and z, and the corresponding velocity components are denoted by u, v, and w, respectively. Additionally, x' and y' are the horizontal and diagonal wall-parallel coordinates, respectively. The ducts have a fixed streamwise length of $L_z = 20\pi\delta$, where δ is the duct half-height, and the slanted-duct sidewall lengths are $L_{x'} = L_{y'} = 2\delta$.

When a slant angle α is applied to the duct, two opposing corner angles decrease by α, while the remaining two increase by α. The side lengths $L_{x'}$ and $L_{y'}$ are maintained constant, resulting in a rhombic cross-section. Three test cases with slant angles $\alpha = 15^\circ$, 30°, and 45° are examined. Each case is simulated at a friction Reynolds number of $Re_\tau = w_\tau D_h/\nu = 300$, where D_h, w_τ, and ν denote the hydraulic diameter, friction velocity, and kinematic viscosity, respectively. As the slant angle increases, the cross-sectional area A decreases. To enable a fair comparison, the hydraulic

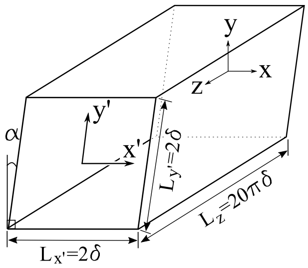

Figure 1: Schematic diagram of the flow domain.

diameter $D_h = 4A/P$, is adopted as the characteristic length scale, where P and A are the duct perimeter and cross-sectional area, respectively. The flow is fully developed, and a periodic boundary condition is applied in the streamwise direction. A no-slip boundary condition is enforced at all solid walls. The continuity and momentum equations governing the incompressible flow read

$$\frac{\partial u_i}{\partial x_i} = 0 \quad , \tag{1}$$

$$\frac{\partial u_i}{\partial t} + u_j \frac{\partial u_i}{\partial x_j} = -\delta_{i3}\frac{\Pi}{\rho} - \frac{1}{\rho}\frac{\partial p}{\partial x_i} + \nu \frac{\partial^2 u_i}{\partial x_j \partial x_j} \quad , \tag{2}$$

where u_i, ρ, ν, p and δ_{ij} denote the velocity, density, kinematic viscosity, pressure, and the Kronecker delta, respectively. The flow is driven by a constant mean streamwise pressure gradient Π. The cross-stream area of the slanted duct decreases as the slant angle increases, the streamwise pressure gradient Π is fine-tuned to maintain a constant Re_τ.

The DNS was conducted using the spectral-element code "Semtex" (Blackburn & Sherwin, 2004), which was developed in C++ and FORTRAN and parallelized using Message Passing Interface (MPI) libraries. The code is highly accurate and well suited to conduct high fidelity DNS studies. The numerical method combines the accuracy of spectral methods with the geometric flexibility of finite-element methods.

The cross-stream plane is divided into 484, 576, and 900 quadrilateral finite elements for the 15°, 30°, and 45° cases, respectively. Each element is further discretized using an 8th-order Gauss–Lobatto–Legendre Lagrange (GLLL) polynomial. The mesh is then extended into the streamwise direction using 1024 Fourier modes for each test case. To capture the sharp gradients in the near-wall region, the grid spacing in the spanwise and vertical directions of the first node off the wall is fixed to $\Delta x^+_{\min} = \Delta y^+_{\min} = 0.07$. In this study, the superscript $(\cdot)^+$ denotes inner scaling using ν and w_τ. The streamwise grid spacing is uniform, with $\Delta z^+ \approx 10$ for each test case. The grid resolution of each test case is summarized in Table 1. A precursor simulation was run until the flow became statistically stationary, after which 900 instantaneous flow fields were collected for all test cases. All simulations and data storage were performed on the Grex supercomputers at the University of Manitoba.

In this study, instantaneous variables (e.g., w) are decomposed into their mean $\langle w \rangle$ and fluctuating w' components, such that $w = \langle w \rangle + w'$. Here $\langle \cdot \rangle$ denotes averaging over time and in the z direction. In smooth- and slanted-duct flows, the friction velocity varies along the duct perimeter. The local time- and streamwise-averaged friction velocity is defined as $w_{\tau,l} = \sqrt{\tau_w/\rho}$, where $\tau_w = \nu \partial \langle w \rangle / \partial n$ is the local wall viscous shear stress and n denotes the wall-normal coordinate. The time- and surface-averaged wall friction velocity is defined as $w_{\tau,a} = \sqrt{\langle \oint_P (\tau_w/\rho)\, dl/C \rangle}$, where the integration is performed over the perimeter P of the cross-section, and C denotes the duct perimeter. The quantity $w_{\tau,a}$ facilitates comparison among the slanted ducts, as it is independent of peripheral position and varies exclusively with the applied pressure gradient Π.

Table 1: Test cases and grid resolutions.

α	D_h	N_x	N_y	N_z	$\Delta x^+_{\min}$
15°	1.931	177	177	1024	0.07
30°	1.732	198	198	1024	0.07
45°	1.414	241	241	1024	0.07

Table 2: Summary of duct metrics.

α	Re_τ	Re^a_τ	$W_b/W_{b,0°}$	C_D
0°	300	314	1	0.00929
15°	300	312	1.034	0.00991
30°	300	305	1.164	0.00927
45°	300	308	1.450	0.00810

RESULTS AND DISCUSSION

Table 2 presents the nominal friction Reynolds number Re_τ, the actual friction Reynolds number Re^a_τ, and the drag coefficient C_D, which are defined as

$$Re^a_\tau = \frac{w_{\tau,a} D_h}{\nu} \quad , \tag{3}$$

$$C_D = \frac{1}{A_w}\int_{A_w} C_f \, dA = 2\left(\frac{w_{\tau,a}}{W_b}\right)^2 \quad , \tag{4}$$

where A_w, C_D, and W_b denote the duct wetted area, drag coefficient, and bulk velocity, respectively. By comparing the smooth- and slanted-duct flows, it is observed that the magnitude of the drag coefficient increases by 6.67% for $\alpha = 15°$ and is essentially the same for $\alpha = 30°$. By contrast, when $\alpha = 45°$, the drag coefficient decreases by 12.81%, demonstrating a substantial reduction of hydraulic losses.

Figure 2 shows contours of the mean streamwise velocity normalized by the average friction velocity $w_{\tau,a}$, superimposed with streamlines of the mean cross-stream velocity ($\langle u \rangle$ and $\langle v \rangle$). Due to the antisymmetry about the diagonal wall-parallel coordinate y'/δ, only half of the domain for each test case is presented. As seen in Fig. 2(a) there exists a pair of counter-rotating mean vortices in each corner of the duct. As slant angle increases

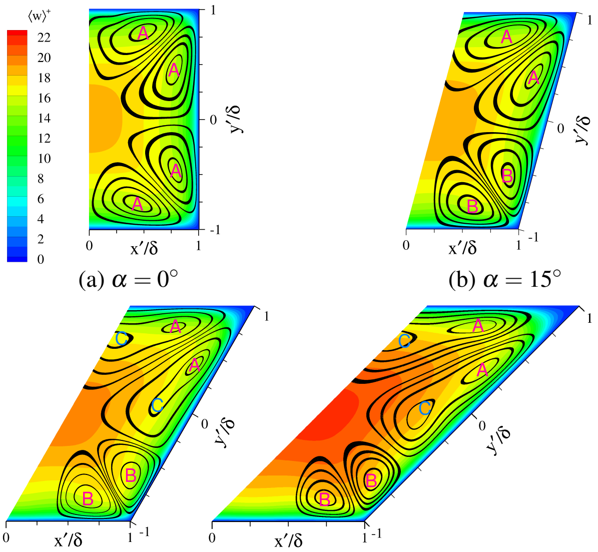

(a) $\alpha = 0°$ (b) $\alpha = 15°$

(c) $\alpha = 30°$ (d) $\alpha = 45°$

Figure 2: Contours of the mean streamwise velocity $\langle w \rangle^+$ non-dimensionalized by $w_{\tau,a}$, super-imposed with streamlines of the mean secondary flows. Due to symmetry, only half of the duct cross-section is shown.

the vortices in the slanted duct are distorted. Specifically, the acute-corner vortices (denoted by "*A*") are elongated, while the obtuse-corner vortices (denoted by "*B*") are compressed. This distortion arises from the differing boundary-layer interactions, which create a need for larger cross-stream motions in the acute corner to compensate for the increased momentum deficit. Interestingly, as the slant angle increases, the acute-corner vortices split, giving rise to a second weaker vortex (labeled "*C*" in Figs. 2(c) and (d)).

Figure 3 presents profiles of the non-dimensionalized mean streamwise velocity $\langle w \rangle^+$ along y'/δ at $x'/\delta = 0$ and $x'/\delta = 0.5$. As expected, the profiles extracted at $x'/\delta = 0$ are symmetric and trivial. This symmetry is not observed for the profiles extracted at $x'/\delta = 0.5$, as velocity is simultaneously dampened in the acute corner and enhanced in the obtuse corner. It is interesting to observe that the velocity in the vicinity of the obtuse corner increases monotonically as α increases, while a more complicated relationship is observed in the duct core and acute corner regions. The non-monotonic trend of velocity in these regions is highly dependent on the splitting of the mean vortex structures observed (see Fig 2).

Figure 4 shows profiles of the spanwise velocity non-dimensionalized by the bulk velocity, along y'/δ at $x'/\delta = 0.5$ and $x'/\delta = 0.75$. Comparing Figs. 4(a) and (b), in the obtuse corner, the near-wall minimum of the spanwise velocity at higher slant angles seems to migrate from $x'/\delta \simeq 0.5$ towards $x'/\delta \simeq 0.75$. Meanwhile, in the acute corner the near-wall minimum tends to maintain a position at $x'/\delta \simeq 0.5$. Furthermore, the boundary between the acute- and obtuse-corner mean-flow structures can be identified from the central local minimum of each profile. This boundary shifts toward the obtuse corner as the slant angle increases, clearly

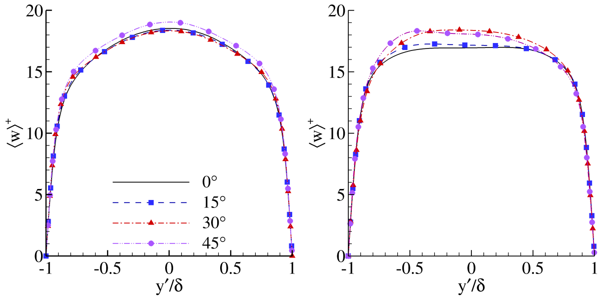

(a) $x'/\delta = 0$ (b) $x'/\delta = 0.5$

Figure 3: Profiles of $\langle w \rangle^+$ along y'/δ at $x'/\delta = 0$ and 0.5. The profiles are non-dimensionalized by $w_{\tau,l}$.

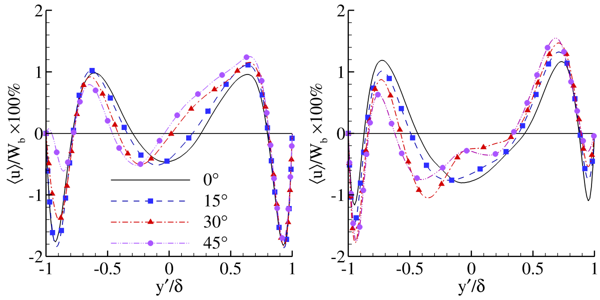

(a) $x'/\delta = 0.5$ (b) $x'/\delta = 0.75$

Figure 4: Profiles of the spanwise velocity along y'/δ at $x'/\delta = 0.5$ and 0.75. The profiles are non-dimensionalized as $\langle u \rangle / W_b \times 100\%$.

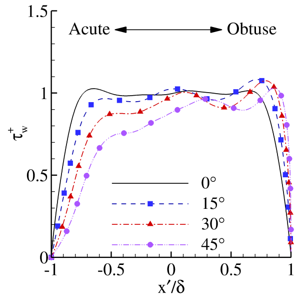

Figure 5: Wall shear stress along the bottom wall, non-dimensionalized by $w_{\tau,a}$

compressing the obtuse-corner flow and stretching the acute-corner flow.

Figure 5 shows the wall shear stress along the bottom wall, non-dimensionalized by the average friction velocity ($w_{\tau,a}$). In the smooth-duct flow, the wall shear stress is zero in the corner and largest at the wall center. As slant angle increases, the wall shear stress skews toward the obtuse corner, diminishing in the acute corner with a marginal increase in the obtuse corner. This comes as a result of two mechanisms. Firstly, the increased boundary layer interaction dampens momentum in the acute corner, and the opposite occurs in the obtuse corner. Secondly, high-momentum fluid is drawn into the near-wall region of the obtuse corner by the mean secondary flow.

Figure 6 shows the profiles of the streamwise velocity scaled using the local friction velocity. Increasing slant angle causes the velocity profiles to deviate from the linear law ($\langle w \rangle^+ = y^+$). Clearly, the increased interaction of the boundary layers at higher slant angles shifts

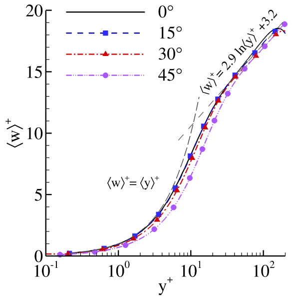

Figure 6: Law of the wall scaled with the local friction velocity $w_{\tau,l}$ at $x'/\delta = 0$.

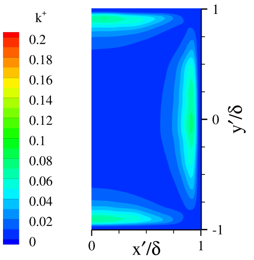

(a) $\alpha = 0°$

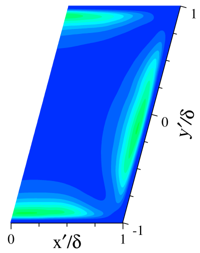

(b) $\alpha = 15°$

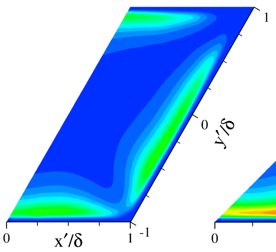

(c) $\alpha = 30°$

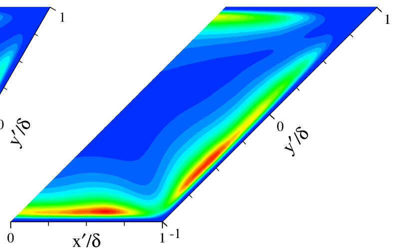

(d) $\alpha = 45°$

Figure 7: Contours of the TKE non-dimensionalized by $w_{\tau,a}$. Due to symmetry, only half of the duct cross-section is shown.

the profiles farther away from the log law postulated by Gavrilakis (1992).

Figure 7 presents contours of the TKE, defined as $k = 0.5(\langle u'^2\rangle + \langle v'^2\rangle + \langle w'^2\rangle)$, non-dimensionalized by the average friction velocity. As the slant angle increases, the point of max TKE shifts toward the obtuse corner. Additionally, the $\alpha = 45°$ case exhibits a substantially higher magnitude than the 15° and 30° cases.

Figure 8 shows profiles of the TKE non-dimensionalized by the local friction velocity. In the square-duct flow, the TKE peaks near the wall, and is small in the duct center and at the wall. In slanted-duct flows the peaks of the TKE increase with slanting angle. Additionally, asymmetry is observed, slanting angle localizes energy towards the obtuse corner.

Figure 9 shows the non-dimensionalized viscous, turbulent, and total shear stresses of τ_{yz} (i.e. τ^+_{vis}, $-\langle v'w'\rangle^+$ and τ^+_{tot}, respectively) in the square- and slanted-duct flows. The shear stresses are non-dimensionalized by the local friction velocity $w_{\tau,l}$ and the three shear stresses balance as $\tau^+_{tot} = \tau^+_{vis} - \langle v'w'\rangle^+$. At $x'/\delta = 0$ and $x'/\delta = 0.5$ the viscous shear stresses collapse, and dominate in the near-wall region. Meanwhile, the turbulent shear stresses contribute the most in the core of the duct. At $x'/\delta = 0$ the turbulent shear

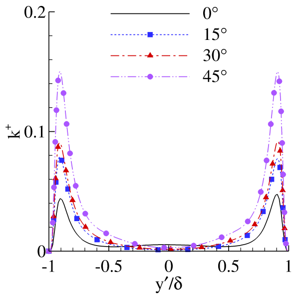

(a) $x'/\delta = 0$

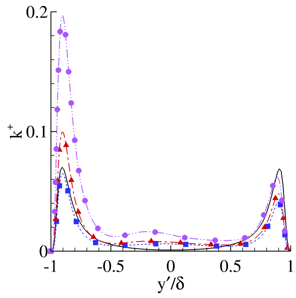

(b) $x'/\delta = 0.5$

Figure 8: Profiles of the turbulent kinetic energy TKE along y'/δ at $x'/\delta = 0$ and 0.5. The profiles are non-dimensionalized by $w_{\tau,l}$.

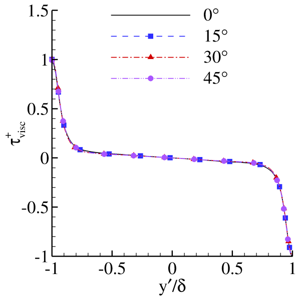

(a) τ^+_{vis}, $x'/\delta = 0$

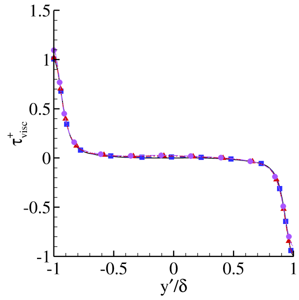

(b) τ^+_{vis}, $x'/\delta = 0.5$

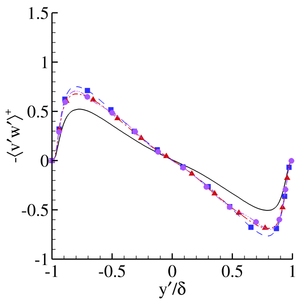

(c) $-\langle v'w'\rangle^+$, $x'/\delta = 0$

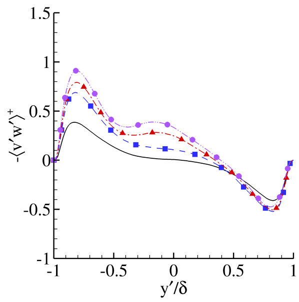

(d) $-\langle v'w'\rangle^+$, $x'/\delta = 0.5$

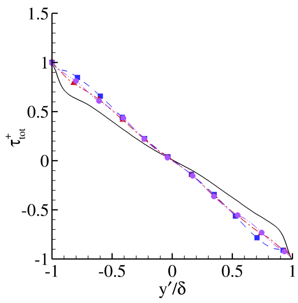

(e) τ^+_{tot}, $x'/\delta = 0$

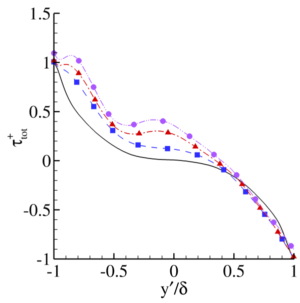

(f) τ^+_{tot}, $x'/\delta = 0.5$

Figure 9: Profiles of τ^+_{vis}, $-\langle v'w'\rangle^+$, and τ^+_{tot} along y'/δ at $x'/\delta = 0$ and 0.5. The profiles are non-dimensionalized using $w_{\tau,l}$.

stress is symmetrical and balances the total shear stress to a linear profile across all test cases. However, at $x'/\delta = 0.5$ the turbulent shear stresses in the slanted-duct flow test cases all exhibit asymmetry, with enhanced magnitudes in the obtuse corner.

To refine the study of slanting effects on the turbulent transport process, the budget balance of the TKE of the square- and slanted-duct flows is investigated. Under the steady flow condition, the TKE transport equation reads

$$\frac{\partial k}{\partial t} = P_k + \Pi_k + H_k + \varepsilon_k + D_k^t + D_k^p + D_k^v = 0 \quad , \qquad (5)$$

where P_k, Π_k, H_k, ε_k, D_k^t, D_k^p, and D_k^v are the production, pressure-strain, convection, viscous dissipation, turbulent diffusion, pressure diffusion, and viscous diffusion terms, respectively, defined as follows:

$$P_k = -\langle u_i' u_j' \rangle \frac{\partial \langle u_i \rangle}{\partial x_j} \quad , \qquad (6)$$

$$\Pi_k = \frac{1}{\rho} \left\langle p' s_{ii}' \right\rangle \quad , \qquad (7)$$

$$H_k = -\frac{1}{2} \langle u_j \rangle \frac{\partial \langle u_i' u_i' \rangle}{\partial x_j} \quad , \qquad (8)$$

$$\varepsilon_k = -\nu \left\langle \frac{\partial u_i'}{\partial x_j} \frac{\partial u_i'}{\partial x_j} \right\rangle \quad , \qquad (9)$$

$$D_k^t = -\frac{1}{2} \frac{\partial}{\partial x_j} \langle u_i' u_i' u_j' \rangle \quad , \qquad (10)$$

$$D_k^p = -\frac{1}{\rho} \frac{\partial}{\partial x_j} \langle p' u_j' \rangle \quad , \qquad (11)$$

$$D_k^v = \frac{1}{2} \nu \frac{\partial^2 \langle u_i' u_i' \rangle}{\partial x_j \partial x_j} \quad . \qquad (12)$$

Figure 10 shows the budget balance of TKE along y'/δ at $x'/\delta = 0$ and 0.5 for each case. Production acts as the primary source term, and dissipation acts as the primary sink. The pressure-strain is zero and the convection and pressure-diffusion terms are negligible, whereas the turbulent- and viscous-diffusion terms act as sources near the wall and sinks away from the wall. In the obtuse corner, enhanced turbulent production P_k^+ is not fully balanced by its reduced rate in the acute corner. This imbalance results from sharper gradients of the mean streamwise velocity ($\partial \langle w \rangle / \partial y$), and the enhanced turbulent shear stress ($-\langle v'w' \rangle^+$) in the obtuse corner shown in (see Figs. 5 and 9(d)).

Additionally, the turbulent-diffusion term D_k^{t+} is stronger in the obtuse corner than in the acute corner, highlighting locally enhanced turbulent mixing. As the slant angle increases, all budget terms increase. This progressive increase in the budget terms with slant angle coincides with the increased TKE shown in Figures 7 and 8. Interestingly, the budget terms in the acute corner for each case diminish to a similar level, with the production decreasing to $P_k^+ \simeq 25$.

Figure 11 shows profiles of the streamwise premultiplied energy spectra calculated at $y'/\delta = -0.9$ and $x'/\delta = 0$, -0.5, 0.5 and 0.75. Across the square- and slanted-duct flows, regardless of cross-sectional location, the characteristic length scales are similar, with the energy (i.e. $\kappa_z^+ E_{ww}^+$) peaking at similar wavelengths, and a majority of the energy concentrated in the same wavelength range ($\lambda_z^+ = 2$ to 40). Figures 11(a) and (b) are taken at duct-wall center and in the vicinity of the acute corner, respectively. Comparing the duct-wall center to the acute-corner, the energy is dampened in the vicinity of the acute corner but maintained at the same level across all test cases. Furthermore, examining the obtuse-corner flow (Fig. 11(c)) reveals that, as slant angle increases, the energy in the obtuse corner increases.

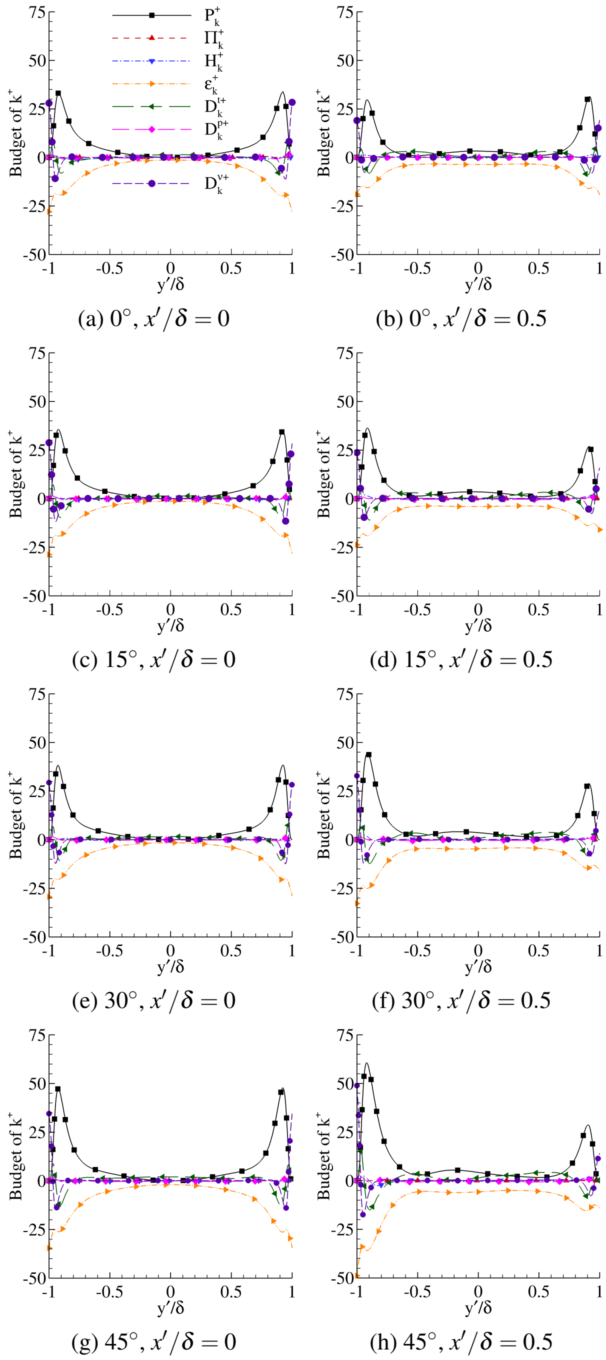

Figure 10: Profiles of the turbulent kinetic energy budget balance along y'/δ at $x'/\delta = 0$ and 0.5. Locations for each test case. All terms are non-dimensionalized by $w_{\tau,l}$.

Interestingly, the obtuse corner exhibits an increased energy level at smaller wavelengths ($\lambda_z^+ = 0.1$ to 2). This marginal shift demonstrates how slanting effects the energy cascade, not only channeling energy into the vicinity of the obtuse corner, but also into a wider range of wavelengths in the obtuse corner. Furthermore, the energy is channeled deeper into the obtuse corner as the slant angle increases. Evidenced in Fig. 11(d), the higher-slant-angle cases maintain a high energy farther into the corner.

Figures 12(a) to (d) compare the vortex structure of each test case. The coherent structures are visualized using the instantaneous swirling strength (λ_{ci}) non-dimensionalized using $w_{\tau,a}$ and ν, and coloured by the

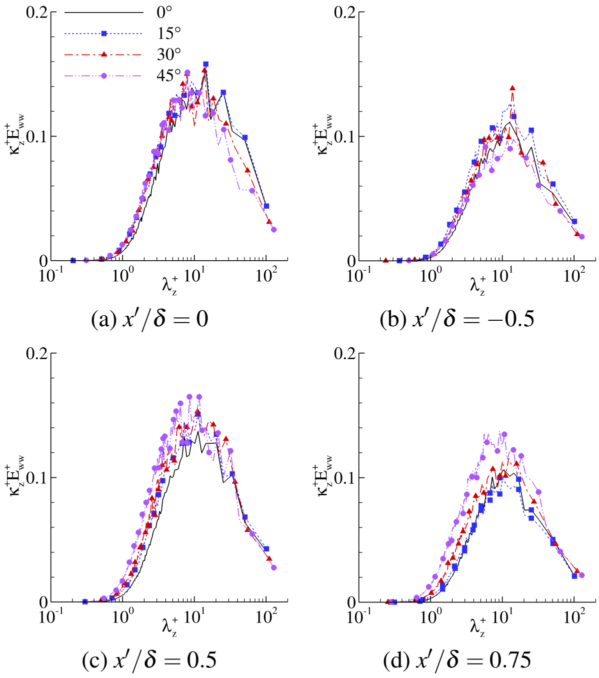

Figure 11: Profiles of the non-dimensionalized streamwise premultiplied energy spectra $\kappa^+ E^+_{ww}$. The profiles are calculated at $y'/\delta = -0.9$ and $x'/\delta = 0$, -0.5, 0.5 and 0.75.

non-dimensionalized instantaneous streamwise velocity w/W_b. For a meaningful comparison, the structures are visualized by setting $\lambda^+_{ci} = 4.5$ for all test cases. In the square-duct flow the structures are clustered near the duct walls, and are evenly dispersed. In the slanted-duct flow the structures are more densely packed in the vicinity of the obtuse corner than in the acute corner, and as slant angle increases from $\alpha = 15°$ to $45°$ the overall density of the flow structures increases.

CONCLUSION

Direct numerical simulations were performed to examine turbulent slanted-duct flow with slant angles of $\alpha = 15°$, $30°$ and $45°$ at $Re_\tau = 300$. Slanting has a clear effect on the mean secondary flows. Compared with the orthongonal square duct, the mean vortices in the acute corner become stretched, while those in the obtuse corner become compressed.

Interestingly, the total drag coefficient C_D is observed to decrease as slant angle increases from $\alpha = 15°$ to $45°$. All of the statistics examined exhibit increased magnitudes in the vicinity of the obtuse corner with a corresponding decrease in magnitude in the vicinity of the acute corner. Notably, the TKE exhibits this behavior, attributed to the enhanced production in the vicinity of the obtuse corner, driven by sharper gradients of the mean streamwise velocity ($\partial\langle w\rangle/\partial y$) and enhanced turbulent shear stress ($-\langle v'w'\rangle^+$). Visualization of the turbulence structures using the swirling strength λ^+_{ci} show that turbulent structures are more densely packed in the vicinity of the obtuse corner than in the acute corner, and as slant angle increases from $\alpha = 15°$ to $45°$ the overall density of the flow structures increases.

Overall, the study shows that duct slant angle strongly affects the secondary flows, turbulence structures, and momentum transport, and should be considered carefully in the design and analysis of slanted-duct flow.

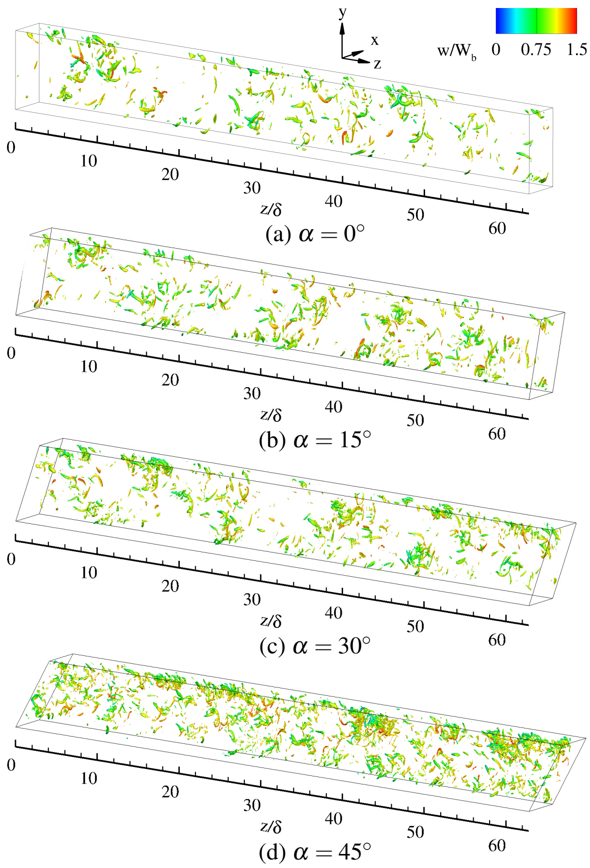

Figure 12: Vortex structures for each test case visualized using the non-dimensionalized swirling strength λ^+_{ci}, and coloured with the non-dimensionalized instantaneous streamwise velocity w/W_b. The swirling strength for each case is set to $\lambda^+_{ci} = 4.5$. The Swirling strength is non-dimensionalized by $\nu/w^2_{\tau,a}$. Due to symmetry, only half the duct cross-section is shown.

REFERENCES

Blackburn, H. M. & Sherwin, S. J. 2004 Formulation of a galerkin spectral element fourier method for three-dimensional incompressible flows in cylindrical geometries. *J. Comput. Phys.* **197**, 759–778.

Fukushima, N. & Kasagi, N. 2003 Heat transfer and friction characteristics in turbulent rhombic duct flows. In *National Heat Trans. Symposium of Japan*.

Gavrilakis, S. 1992 Numerical simulation of low-reynolds-number turbulent flow through a straight square duct. *J. Fluid Mech.* **244**, 101–209.

Gessner, F. B. & Jones, J. B. 1973 The origin of secondary flow in turbulent flow along a corner. *J. Fluid Mech.* **23**, 689–713.

Huser, A., Biringen, S. & Hatay, F. 1994 Direct simulation of turbulent flow in a square duct: Reynolds-stress budgets. *Phys. Fluid.* **6** (9), 3144–3152.

Nikitin, N. & Yakhot, A. 2005 Direct numerical simulation of turbulent flow in elliptical ducts. *J. Fluid Mech.* **532**, 141–164.

Raiesi, H., Pollard, A. & Piomelli, U. 2011 Direct numerical simulations of turbulence induced secondary motion in square and skewed ducts. In *Proceedings of 7th Intl. Heat Transf. Conf.*, *Session 1D*, vol. 1.

Vinuesa, R., Noorani, A., Lozano-Durán, A., El Khoury, G. K., Schlatter, P., Fischer, P. F. & Nagib, H. M. 2014 Aspect ratio effects in turbulent duct flows studied through direct numerical simulation. *J. Turbul.* **15**, 677–706.